PCCP

Shape-preserving conversion of calcium carbonate tubes to self-propelled micromotors

Journal:	*Physical Chemistry Chemical Physics*
Manuscript ID	CP-ART-04-2022-001807.R1
Article Type:	Paper
Date Submitted by the Author:	27-May-2022
Complete List of Authors:	Wang, Qingpu; Florida State University, Department of Chemistry and Biochemistry Steinbock, Oliver; Florida State University, Department of Chemistry and Biochemistry

ARTICLE

Shape-preserving conversion of calcium carbonate tubes to self-propelled micromotors†

Qingpu Wang [a] and Oliver Steinbock*[a]

sReceived 00th January 20xx,
Accepted 00th January 20xx

DOI: 10.1039/x0xx00000x

The self-assembly of inorganic structures beyond the euhedral shape repertoire is a powerful approach to grow hierarchically ordered materials and mesoscopic devices. The hollow precipitate tubes in chemical gardens are a classic example, which we produce on Nafion membranes separating a $CaCl_2$-containing gel from a Na_2CO_3 solution. The resulting $CaCO_3$ microtubes are conical and consist of either pure vaterite or calcite. The process also forms branched T- and Y-shaped structures. The metastable vaterite polymorph can be converted to Mn-based structures without loss of the macroscopic shape. In H_2O_2 solution, the resulting tubes self-propel by the release of O_2 bubbles, which for branched structures causes rotation. The tubes can contain multiple bubbles which are ejected in a quasi-periodic fashion (e.g. in groups of four). The addition of surfactants causes the accumulation of bubble trails and bubble rafts that interact with the moving tubes and give rise to distinct motion patterns.

Introduction

The research field of chemobrionics explores meso- and macroscopic shapes that self-organize during inorganic precipitation reactions undergoing complex reaction-transport processes.[1,2] Formed under far-from-equilibrium conditions, these three-dimensional structures strongly deviate from euhedral shapes, appear often life-like, and are in some cases hierarchically ordered. These features suggest deeper links to biomineralization, but they do not rely on biomolecules or biological control mechanisms. The most prominent examples are "chemical gardens" which comprise various tubular precipitation structures that—in the classical version of the experiment—emerge when metal salts are exposed to sodium silicate solution. During the past two decades, numerous modifications of the classical experiment have been developed including the replacement of the seed crystal by injected solutions and tube growth in silicate-free systems.[3,4] Also different potential applications have been demonstrated such as the growth of osteoblasts on calcium phosphate tubes[5] and the incorporation of quantum dots into zinc (hydr)oxide tubes[6]. Despite this progress, the production of a desired tube material often cannot be combined with the selection of a particular tube shape and size. It is hence worth exploring whether the macroscopic precipitate structures can be preserved under chemical transformations such as ion-exchange reactions.[7] To date, the only example of such a shape-preserving transformation has been the thermal conversion of silica-metal hydroxide tubes to silica-metal-oxide tubes.[8,9] For much smaller objects, ion-exchange conversion has been reported for unassembled nanoparticles[10,11] and self-assembled nanocomposites[12-14]. For instance, 50 µm-large, coral-like nanocomposites of $BaCO_3$ were successfully transformed to product materials such as perovskites.[15] Here, we applied these techniques to chemical garden tubes which are much larger at the hierarchical levels of both constituting crystals and overall aggregate shapes.

The concrete motivation for our study was the production of self-propelled microtubes. Such micromotors often operate by the ejection of gas bubbles, can carry cargo, and remove pollutants, which suggests powerful applications in biomedicine and environmental science.[16-20] However, the widespread use of such motors has been limited by the complexity and expense of their fabrication techniques (e.g. physical vapor deposition and electrochemical methods).[21-23] In a recent study, we produced self-propelled cylindrical tubes based on chemical garden growth and a facile injection method.[24] Here, we miniaturized the resulting structures using cation-exchange membranes and expand the available shape repertoire to include structures that were otherwise inaccessible. The as-prepared $CaCO_3$ microtubes were conical, cylindrical, or branched, and readily transformed to Mn-containing structures. This study also opens new avenues for other post-synthetic modifications and related catalytic as well as photochemical applications.

---

[a] *Department of Chemistry and Biochemistry
Florida State University
Tallahassee, Florida 32306-4390 (USA)*
[*] *E-mail: osteinbock@fsu.edu.*

†Electronic Supplementary Information (ESI) available. See DOI: 10.1039/x0xx00000x

Experimental

Chemicals and materials

Calcium chloride ($CaCl_2$, EMD Millipore Corp), manganese chloride ($MnCl_2 \cdot 4H_2O$, Fisher Chemical), sodium carbonate ($Na_2CO_3 \cdot H_2O$, J. T. Baker), hydrogen peroxide (H_2O_2, 30% w/v, VWR Chemicals), agar (Sigma-Aldrich, product number A7002), and bis(2-ethylhexyl) sulfosuccinate sodium salt (AOT, 96 %; Alfa Aesar) were used as received. The ion exchange membrane (Nafion 117) was purchased from the Fuel Cell Store. All solutions were prepared with nanopure water filtered by a Barnstead Easypure UV system (resistivity: 18 MΩ cm).

Tube formation

$CaCO_3$ tubes were produced according to a novel protocol that modifies a previously reported solution-solution method[25]. First, we prepared a 1% w/w agar solution containing 1.0 M $CaCl_2$. 3 mL of the hot viscous liquid was then transferred to a plastic Petri dish (inner diameter: 36 mm). After cooling down to room temperature, the liquid solidified as a translucent gel. A small piece of the cation-exchange membrane (thickness 183 µm, 2×2 cm^2) was rinsed with DI water and placed on top of the gel. Air bubbles between the membrane and gel were carefully chased out. Then, we added an equal volume of 1.0 M Na_2CO_3 solution onto the membrane. The dish was covered with a lid and sealed with Parafilm to avoid the diffusion of CO_2 from the outside air and the loss of water through evaporation.

After one day at room temperature, we decanted the Na_2CO_3 solution and extracted the microstructure-covered Nafion membrane from the Petri dish. A large number of $CaCO_3$ structures were exfoliated from the membrane, rinsed with DI water, and stored in water in a sealed container. Note that the as-prepared $CaCO_3$ structures tended to slowly dissolve in open containers.

Tube conversion

In the typical experiment, the $CaCO_3$ microstructures were first transferred to a glass Petri dish (diameter 50 mm) and excess water was removed. Then, 10 mL of 10 mM $MnCl_2$ solution was added to the Petri dish. The converted structures were extracted and washed at different times to obtain partially converted and/or oxidized structures.

For the time-lapse study, a conical $CaCO_3$ tube was first transferred to a polystyrene Petri dish (diameter 36 mm) and left to dry in the fume hood. Then, 3 mL of 10 mM $MnCl_2$ solution was added to the dish and the tube was centered in the field of view on the stage of an optical microscope (Leica, DM IRB). We collected micrographs every 2 min for several days using a camera (Nikon D3300). For this purpose, the camera was connected to a PC and controlled with the program digiCamControl.

Characterization

Both freshly prepared and converted tubes were washed and dried on a glass slide before further characterization. Micro-Raman spectroscopy was carried out using a Horiba JY LabRam HR Evolution spectrometer at an excitation wavelength of 633 nm (HeNe laser).

Samples were coated with a 4.0 nm layer of iridium prior to characterization by scanning electron microscopy (SEM, FEI Nova 400 operating at 10 kV) and energy dispersive X-ray spectroscopy (EDS, Oxford 100 mm^2 UltimMax SDD detector). Tube samples from six different experiments were collected for the powder X-ray diffraction (XRD) studies. These measurements employed a Rigaku SmartLab diffractometer with a copper X-ray source.

Results and discussion

Producing hollow $CaCO_3$ structures

We produced $CaCO_3$ tubes on cation-exchange membranes placed between a Na_2CO_3 solution and an agar gel containing $CaCl_2$ (Fig. 1a). After one day, numerous hollow $CaCO_3$ microstructures formed on the membrane and grew into the Na_2CO_3 solution. When we extracted the square membrane from the Petri dish and dried it under ambient conditions, the membrane curled into a cylindrical shape exposing elongated $CaCO_3$ structures extending away from the surface (Figs. 1b and S1). Figures 1c,d show optical micrographs of these tubes including conical, cylindrical, T-shaped, and Y-shaped structures (see Fig. S2 for more examples in the ESI†).

Micro-Raman spectra of the dried tubes (Fig. 1e) showed characteristic peaks that correspond to calcite[26] (153, 278, 711, 1084 cm^{-1}) and vaterite[27] (106, 209, 268, 300, 740, 751, 1074, 1090 cm^{-1}). These product materials are polymorphs of $CaCO_3$ with calcite being the thermodynamically most stable form and vaterite being metastable.[28] The XRD pattern of the ground tubes that were randomly selected (Fig. S3, ESI†) also confirmed this composition and yielded a calcite-to-vaterite ratio of 61:39.[29,30] Optical microscopy employing a dark-field-like illumination revealed different scattering signatures. One group of tubes strongly scattered obscuring the hollow tube core, while another was more transparent (Fig. S2, ESI†). If tubes were sorted accordingly, the sample populations corresponded cleanly to calcite (strong light scatters) and vaterite (more transparent) (Fig. 1e). Therefore, the overall polymorph ratio is caused by two distinct tube populations, not a mix within individual tubes. The differences in the scattering behavior are linked to different microscale textures observed by SEM (Figs. S4,S5, ESI†). The vaterite tubes showed a smooth surface, whereas the calcite tubes consisted of rectangular crystals that were stacked along the tube axis.

Both calcite and vaterite tubes were conical but differed in size and opening angle (Figs. 1c,d). The more slender calcite tubes typically had radii of 15 µm at the tip and lengths of 1 to 3 mm. In comparison, the vaterite tubes had larger tip radii of 40 µm and shorter lengths of 0.8 to 1.3 mm. While for the majority of the tubes, the radius decreased with increasing distance from the Nafion membrane, some had a reverse orientation and were reliably closed at the wide, distant end. The latter tubes always consisted of calcite. Another type of hollow structure featured junction points among three tube segments of which two often appeared like a sharply bent tube with the third arm emerging from the bend. All of these three-armed structures consisted of vaterite. Notice that for unstructured (i.e. non-tubular) $CaCO_3$ particles, the polymorph ratios can be controlled by temperature variations [31], which suggests the possibility of polymorph control for the entire batch of microtubes.

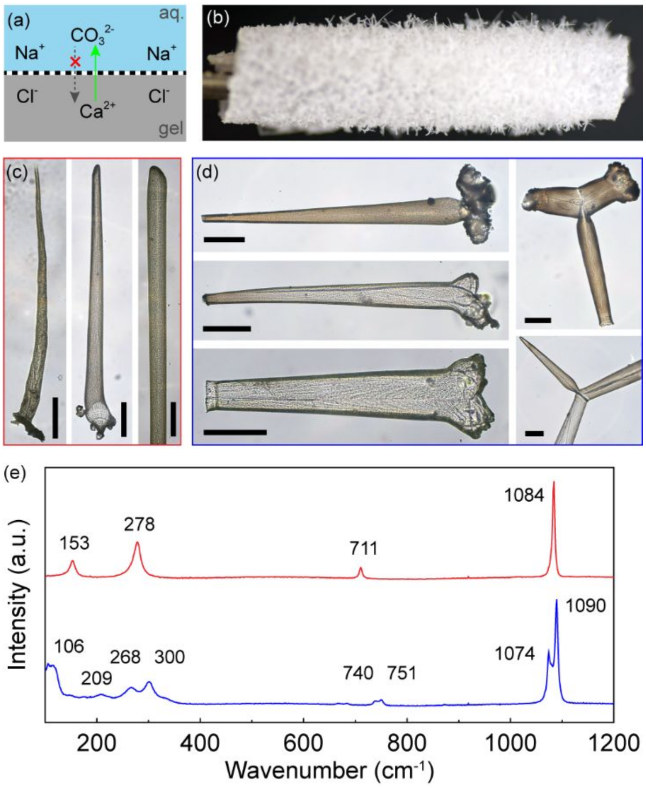

Fig. 1 (a) Schematics of the experimental setup. A cation-exchange membrane (Nafion) was placed between an upper Na_2CO_3 solution and a lower gel containing $CaCl_2$. (b) Photograph of the dried membrane with a thick layer of self-organized $CaCO_3$ microstructures. (c,d) Optical micrographs of different hollow $CaCO_3$ tubes. All scale bars correspond to 200 µm. (e) Micro-Raman spectra of the as-prepared tubes. The red and blue colors correspond to the colors of the image borders in (c,d).

Ca-to-Mn Conversion

We now discuss the shape-preserving conversion of the $CaCO_3$ microstructures to manganese-containing products with the last paragraph of the section addressing the nature of the product materials. For this transformation, we immersed—under ambient conditions—freshly prepared tubes in 10 mM $MnCl_2$(aq). The sequence of optical micrographs in Fig. 2a shows a $CaCO_3$ tube that gradually changed from white to brown during the cation exchange (also see Movie S1 and Figs. S6,S7, ESI†). The brown tubes obtained after 24 hours of conversion remained optically transparent; longer exposure to the $MnCl_2$ solution resulted in black, opaque tubes. We observed that these color changes started from the ends of the tube and spread in a front-like fashion towards the middle of the structure. This space-dependent delay of the transformation process is captured in the time-space plot of Fig. 2b and is likely due to oxygen diffusion within the tube cavity. In addition, some structures experienced tip dissolution which slightly decreased the tube length.

SEM images of the brown tubes (Figs. 2c,d) showed a surface texture similar to that of the white vaterite tubes (Fig. S5, ESI†). Furthermore, cross-sectional views revealed transmural fibers that span the entire 4-8 µm thick wall (c). This fibrous texture was absent in the black tubes, which often featured 2 µm large, cubic crystals on the outer surface (e). The micro-Raman measurements of these crystals (Figs. S8, ESI†) indicate that they possibly consisted of both calcite and $MnCO_3$. The interior surface of the brown tubes was remarkably smooth (d), whereas black tubes revealed a slightly undulating, bumpy texture (f).

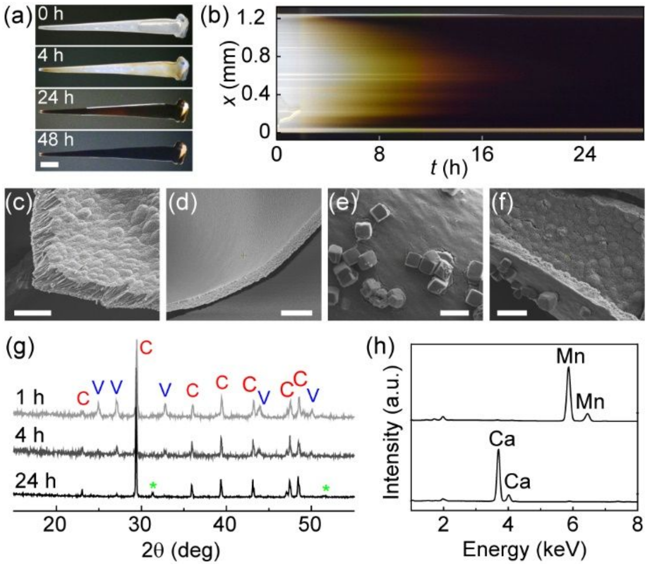

Fig. 2 (a) Schematics of the tube conversion. (a) Optical micrographs of the same conical tube in 10 mM $MnCl_2$ solution after 0, 4, 24, and 48 h. Scale bar: 200 µm. (b) Time-space plot along the tube's axis. (c-f) SEM images of the tube after 4 h (light brown) and 96 h (black) of conversion. (c,e) Exterior surfaces; (d,f) interior surfaces. Scale bars: 10 µm (c, d, g) and 5 µm (f). (g) Powder XRD patterns of ground tubes for different conversion times. The peaks labeled V and C correspond to vaterite and calcite, respectively. The green asterisks mark the possible signals of $MnCO_3$ (Fig. S10). (h) EDS spectra of the brown (lower curve) and black tubes (upper curve).

In order to confirm and quantify the successful conversion of $CaCO_3$ tubes, we characterized samples for different conversion times using powder XRD (Figs. 2g, S9a, and S10). Our measurements showed that the calcite peaks in the diffraction patterns stayed nearly the same over 24 h of $MnCl_2$ exposure, while the vaterite signal gradually disappeared. We also observed that the calcite tubes stayed white after 3 days in 10 mM $MnCl_2$ (Fig. S11 and Movie S2, ESI†). Based on these observations, we conclude that—over the studied time interval—the calcite tubes do not undergo the Ca^{2+}-to-Mn^{2+} exchange reaction whereas the vaterite tubes do. Notice that also an increase of $MnCl_2$ concentration to 100 mM left the calcite tubes unchanged even after 3 days. Due to the lower solubility of $MnCO_3$ compared to $CaCO_3$, we believe that, given proper conditions (e.g., at elevated temperatures), such an ion-exchange process for calcite will become more noticeable.

For vaterite tubes exposed to $MnCl_2$ solutions, we performed energy dispersive spectroscopy (EDS) measurements that yielded mass percentages of 97.1% Ca and 2.9% Mn after 4 h. The brown color of these tubes is hence not an appropriate indicator of a high Mn content. This result is confirmed by micro-Raman spectra which showed nearly unchanged intensities of the vaterite peaks (Fig. S10b, ESI†). After 2 days, however, the composition had changed to 0.4% Ca and 99.6% Mn indicating a nearly complete replacement (Figs. S12,S13 ESI†). We attribute the polymorph-specific susceptibility to ion replacement to the higher solubility[32,33] of the metastable vaterite, but other features such as a possibly larger porosity of the vaterite tubes might be contributing factors.

We now discuss the difficult question of the nature of the material(s) that result from the vaterite tube conversion. Raman spectra unambiguously show the disappearance of the carbonate-specific signal around 1090 cm^{-1} for conversion times of 1 d or more; indeed, no peaks are found between 800 and 1200 cm^{-1} (see Fig. S9b). Accordingly, neither calcium nor manganese carbonate are detected. Moreover, EDS analyses of these materials show large amounts of manganese and essentially no calcium (Fig. 2h). XRD patterns show no additional signals with the exception of a minor $MnCO_3$ signal (Fig. S10), which indicates that the main product material is likely amorphous (the conversion-resistant calcite pattern persists). Further inspection of the Raman spectra reveals new peaks around 501 and 635 cm^{-1}, which could be indicative for one of the many manganese oxides (or oxyhydroxide) or a mixture of those substances.[34] While the synthesis of manganese oxides typically relies on high temperatures, the room temperature synthesis of Mn_3O_4 in the presence of carbonate ions has been reported by Zhang et al.[35] providing indirect evidence for the feasibility of such a reaction in our experiment. As the exact characterization of the product material is secondary to this dynamics-focussed study, we did not attempt to further untangle the exact composition of this amorphous and likely multi-component material.

Self-propulsion

We selected $MnCl_2$ for the conversion process because manganese compounds, especially MnO_2, are known as excellent catalysts for the decomposition of H_2O_2 and hence suitable target materials for micromotors.[36,37] When we placed the converted tubes in 2% w/v H_2O_2, they indeed immediately began to produce bubbles, moved up from the bottom of the solution, and commenced the desired self-propulsion just underneath the water-air interface. The resulting motion is illustrated for a typical conical tube in the bottom row of Fig. 3a (see also Movie S3 in the ESI†). In this example, the 0.7 mm long tube followed a circular path anticlockwise with an average speed of 1.1 mm/s. This movement reliably occurred in the direction of the conical structure's tip. The original $CaCO_3$ tubes do not show self-propulsion in H_2O_2 solutions.

The self-motion of the converted tubes is driven by the ejection of small oxygen bubbles produced by the catalytic decomposition of hydrogen peroxide ($2\ H_2O_2\ (aq) \rightarrow 2\ H_2O\ (l) + O_2\ (g)$) within the tube cavity. In this respect, our tubes share similarities to the polyaniline/metal(oxide) micromotors produced by advanced techniques such as the rolling up of functional nanomembranes on polymers;[21,22,38-40] however, our approach is simpler and both more economical to scale up and potentially versatile with regard to different product materials. The average bubble diameter was comparable to the average tube width and smaller than those reported for large silica-MnO_2 tubes.[24] Due to the lack of an insulating, non-catalytic outer layer, bubbles also formed on the tube exterior.

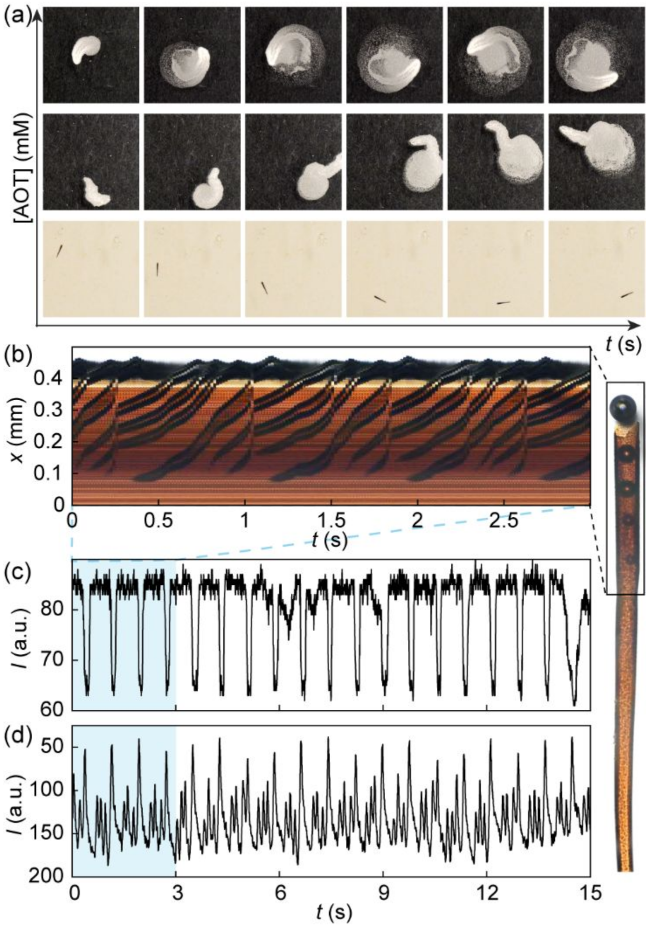

Fig. 3 (a) Image sequences of converted conical tubes moving in 2% H_2O_2 solutions containing 0.5, 0.1, and 0 mM AOT. The white patches are foam-like bubble rafts. Time between frames: 40 s (upper row), 12 s (middle), and 1 s (lower). Field of view: 12 × 12 mm^2 (upper and middle), 5 × 5 mm^2 (lower). (b-d) Time evolution of bubble formation inside a transparent conical tube in 0.05% H_2O_2. The time trace in (c) was obtained at x = 0.08 mm. The intensities in (d) are averages for x = 0.44-0.47 mm.

The oxygen bubbles lingered underneath the water-air interface before bursting, but did not affect the observed tube motion noticeably. To provoke an interaction between the self-propelled tubes and their associated microbubbles, we added a small amount of surfactant (dioctyl sodium sulfosuccinate, AOT) to the H_2O_2 solution.[41] The resulting bubbles had longer lifetimes and accumulated as a foam-like "exhaust" trail closely surrounding the tube and extending along its wake. This finger-like foam structure introduced erratic changes in the propulsion direction and typically reshaped itself into a larger patch of bubbles that was dragged along or even re-penetrated (middle row in Fig. 3a). When we further increased the concentration of AOT (top row), the conical tube together with its comet-like tail underwent a spinning motion around this large patch. The area of the foam patch increased gradually during the first few minutes, but then stayed almost constant (diameter ~9.5 mm) over the following 20 min or more. Qualitatively, the size of component bubbles in the foam decreased as the concentration of AOT was increased from 0.5 to 1.0 mM (Figs. S14,S15, ESI†). We encourage the reader to watch the Movie S3 as the overall dynamics are difficult to capture in an image sequence.

Quasiperiodic bubble dynamics

The micromotors produced by our approach offer additional benefits. The partially converted, brown tubes are both catalytically active and optically transparent, which allowed the direct observation of bubble nucleation and motion within the tube. To demonstrate and analyze this process, we placed the Mn-tubes into a very dilute H_2O_2 solution (0.05%). Under these conditions, the tubes slowly produced oxygen bubbles and remained stationary at the bottom of the solution. Figure 3b shows a time-space plot illustrating the rhythmic nucleation, growth, and release of bubbles (see Fig. S16 for a larger time interval in the ESI†). We generated this plot by measuring a sequence of line profiles along the tube's central axis and then arranged them in chronological order from the left to the right. Each bubble created a slanted band with dark borders as it moved through the tube (Fig. 3b, Movie S4 in the ESI†). At essentially all times, the tube contained four distinct bubbles of different sizes that nucleated at one specific location 0.3 mm away from the wide tube end (total tube length 1.5 mm). The average velocity of the bubbles within the tube is 0.48 mm/s. The horizontal bands in the background reflect structural features of the stationary tube and the brown-to-beige border marks the starting point of the orifice.

To quantify the periodicity of the bubble dynamics, we plotted the intensity of the grayscale time-space plot slightly above the nucleation site (Fig. 3c). The results reveal a nucleation frequency of 0.79±0.03 s. The upper edge of the time-space plot decodes the ejection rhythmicity (Fig. 3d). Surprisingly, this bubble release showed period-4 oscillations[42] in which one large peak is followed by three small ones.

The quasi-periodic behavior of the micromotor is linked to strong fluid flow within the tube immediately after each bubble release. This effect is strongest for the large bubbles and induces a (poorly resolved) sudden upward shift of the trailing gas pockets. Four of these events are shown in Fig. 3b (t = 0.3, 1.0, 1.8, and 2.6 s). The release of the smaller bubbles accelerates the trailing ones more gently, which smoothly increases the slopes of the bands in the time-space plot.

The quasiperiodicity is likely caused by a symmetry-breaking mechanism. We can consider a starting condition for which equally sized bubbles are released at one exact period. This situation may experience a small fluctuation that increases the volume of one bubble. When this bubble is ejected, it will enhance the acceleration of the bubbles already moving within the tube, but not affect their volume. The currently growing bubble, however, inherits the initial perturbation and reaches a larger size due to a stronger influx of fresh solution from the small orifice of the tube. If this effect amplifies the disparity of volumes, a measurable quasiperiodic rhythm is established. The specific nature of this rhythm reflects the average total number of bubbles within the tube, which in Fig. 3b is four and gives rise to period-4 behavior. Accordingly, the—random but static—position of the nucleation site within the tube is of importance for the quasiperiodic release dynamics and, most likely, the propulsion characteristics at higher fuel concentrations.

Branched structures and self-rotation

Our experiments also produced T-shaped tubes that cannot be fabricated using established[20-22,38-39,43] synthetic methods. We identified all of these three-armed structures as vaterite. Therefore, they can be converted by the same ion-exchange process as the conical tube shown in Fig. 2. In H_2O_2 solutions, the T-shaped tubes mainly ejected bubbles from one of the orifices of the linearly connected or slightly bent tube pair (Fig. S17, ESI†). Consequently, they exhibited rotational motion around a center point (Movie S5, ESI†). This point can be located at different distances from the tube, which resulted in distinct rotational modes (Fig. S18, ESI†). One representative mode is shown in Fig. 4a which was constructed by superposing snapshots of the moving tube and encoding the respective times as a specific color. Here, the rotation was counterclockwise, and the stem of the T-shaped structure pointed backward at a constant angle ($\approx 38°$) to the tangent of the circular trajectory. Other modes involved tube stems pointing inwards with respect to the trajectory and for those the center of rotation could be either on the structure or outside (Fig. S18, ESI†). We also observed that the rotational modes of a given tube were dependent on both the H_2O_2 concentration and geometric factors such as the stem-to-bar ratio of the T-shaped structure.

Lastly, we studied the motion of T-shaped structures by tracking the centroid of the structure for longer periods of time. The resulting trajectories revealed a slow drift that consisted of looping arches (Fig. 4b). This drift depends on the specific tubes as well as the employed H_2O_2 concentration (Fig. S19, ESI†) and is at least partly due to bubble formation on the exterior surface. In addition, the total arc length of the trajectory s increases linearly over time indicating a constant speed v (Fig. 4c). Notice that this speed is not the propulsion speed as the primary rotational motion is excluded when tracing the structure's center. For a given tube, v increased proportionally with the H_2O_2 concentration (Fig. 4d) yielding a proportionality constant of k = 16 mm L/(s mol). Proportional dependencies were also found for other T-shaped tubes (Fig. S20, ESI†), but k varied by a factor of up to five.

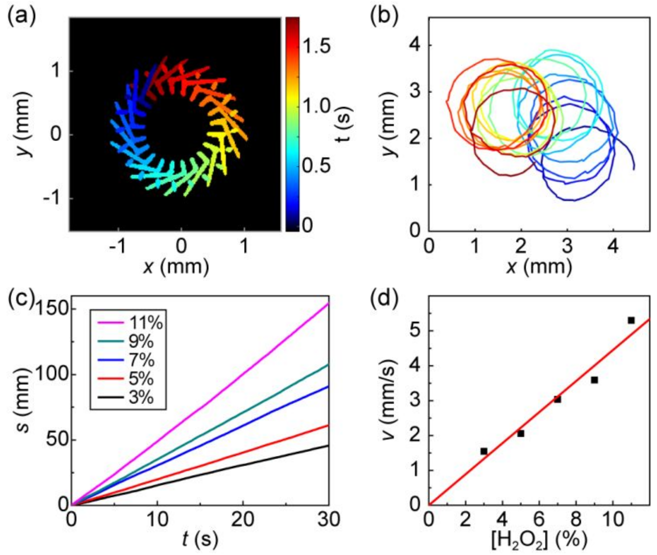

Fig. 4 (a) Image sequences of converted conical tubes moving in 2% H_2O_2 (a) Superposed snapshots of a rotating T-shaped tube in 9% H_2O_2 measured for 1.75 s. (b) Trajectory of the centroid of the same T-shaped tube measured for 25 s. The blue and red colors in (a,b) encode time. (c) Distance traveled by the centroid over time for different H_2O_2 concentrations. (d) Centroid velocity as a function of H_2O_2 concentration (red line is the best proportional fit).

Conclusions

In summary, we modified a membrane-based synthesis method for the facile production of conical and T-shaped calcite and vaterite microtubes. Using the latter, we then demonstrated the first shape-preserving conversion of chemical garden tubes and utilized the resulting structures as self-propelled micromotors. Our experiments revealed complex rotational modes and also suggested the existence of quasiperiodic propulsion dynamics. Future studies could explore the countless possibilities for shape-preserving conversion and functionalization, thus widening the applicable conditions and performance features for their use as microengines.

Conflicts of interest

There are no conflicts to declare.

Acknowledgements

This material is based upon work supported by NASA under grant No. 80NSSC18K1361 and the National Science Foundation under grant No. 1565734. We thank E. Lochner for access to the SEM instruments in the Condensed Matter and Material Physics (CMMP) User Facility at Florida State University. We also thank X. Lin for assistance with powder XRD measurements, B. C. Batista for discussions, and S. Gonzalez, P. Knoll, E. Nakouzi, as well as L. Roszol for performing initial experiments.

Notes and references

1 L. M. Barge, S. S. S. Cardoso, J. H. E. Cartwright, G. J. T. Cooper, L. Cronin, A. De Wit, I. J. Doloboff, B. Escribano, R. E. Goldstein, F. Haudin, D. E. H. Jones, A. L. Mackay, J. Maselko, J. J. Pagano, J. Pantaleone, M. J. Russell, C. I. Sainz-Diaz, O. Steinbock, D. A. Stone, Y. Tanimoto and N. L. Thomas, *Chem. Rev.*, 2015, **115**, 8652-8703.
2 E. Nakouzi and O. Steinbock, *Sci. Adv.*, 2016, **2**, 1-13.
3 S. Thouvenel-Romans, W. v. Saarloos and O. Steinbock, *Europhys. Lett.*, 2004, **67**, 42-48.
4 B. C. Batista and O. Steinbock, *Chem. Commun.*, 2015, **51**, 12962-12965.
5 E. A. B. Hughes, M. Chipara, T. J. Hall, R. L. Williams and L. M. Grover, *Biomater. Sci.*, 2020, **8**, 812-822.
6 R. Makki, X. Ji, H. Mattoussi and O. Steinbock, *J. Am. Chem. Soc.*, 2014, **136**, 6463-6469.
7 B. J. Beberwyck, Y. Surendranath and A. P. Alivisatos, *J. Phys. Chem. C*, 2013, **117**, 19759-19770.
8 J. J. Pagano, T. Bánsági and O. Steinbock, *Angew. Chem. Int. Ed.*, 2008, **47**, 9900-9903.
9 L. Roszol, R. Makki and O. Steinbock, *Chem. Commun.*, 2013, **49**, 5736-5738.
10 B. C. Steimle, J. L. Fenton and R. E. Schaak, *Science*, 2020, **367**, 418-424.
11 J. M. Hodges, K. Kletetschka, J. L. Fenton, C. G. Read and R. E. Schaak, *Angew. Chem. Int. Ed.*, 2015, **54**, 8669-8672.
12 H. C. Hendrikse, A. van der Weijden, M. Ronda-Lloret, T. Yang, R. Bliem, N. R. Shiju, M. van Hecke, L. Li and W. L. Noorduin, *Adv. Mater.*, 2020, **32**, 2003999.
13 H. C. Hendrikse, A. Aguirre, A. van der Weijden, A. S. Meeussen, F. Neira D'Angelo and W. L. Noorduin, *Cryst. Growth Des.*, 2021, **21**, 4299-4304.
14 H. C. Hendrikse, S. Hémon-Charles, L. Helmbrecht, E. P. van Dam, E. C. Garnett and W. L. Noorduin, *Cryst. Growth Des.*, 2021, **21**, 4500-4505.
15 T. Holtus, L. Helmbrecht, H. C. Hendrikse, I. Baglai, S. Meuret, G. W. P. Adhyaksa, E. C. Garnett and W. L. Noorduin, *Nat. Chem.*, 2018, **10**, 740-745.
16 J. X. Li, I. Rozen and J. Wang, *ACS Nano*, 2016, **10**, 5619-5634.
17 W. Gao, R. F. Dong, S. Thamphiwatana, J. X. Li, W. W. Gao, L. F. Zhang and J. Wang, *ACS Nano*, 2015, **9**, 117-123.
18 J. R. Baylis, J. H. Yeon, M. H. Thomson, A. Kazerooni, X. Wang, A. E. St. John, E. B. Lim, D. Chien, A. Lee, J. Q. Zhang, J. M. Piret, L. S. Machan, T. F. Burke, N. J. White and C. J. Kastrup, *Sci. Adv.*, 2015, **1**, e1500379.
19 Z. Z. Li, T. Zhang and K. Li, *Dalton Trans.*, 2011, **40**, 2062-2066.
20 K. Villa, J. Parmar, D. Vilela and S. Sánchez, *ACS Appl. Mater. Interfaces*, 2018, **10**, 20478-20486.
21 Y. Mei, G. Huang, A. A. Solovev, E. B. Ureña, I. Mönch, F. Ding, T. Reindl, R. K. Y. Fu, P. K. Chu and O. G. Schmidt, *Adv. Mater.*, 2008, **20**, 4085-4090.
22 W. Gao, A. Uygun and J. Wang, *J. Am. Chem. Soc.*, 2012, **134**, 897-900.
23 H. Wang and M. Pumera, *Chem. Rev.*, 2015, **115**, 8704-8735.

24 Q. Wang, P. Knoll and O. Steinbock, *J. Phys. Chem. B*, 2021, **125**, 13908–13915.

25 M. Takiguchi, K. Igarashi, M. Azuma and H. Ooshima, *Cryst. Growth Des.*, 2006, **6**, 1611-1614.

26 S. P. S. Porto, J. A. Giordmaine and T. C. Damen, *Phys. Rev.*, 1966, **147**, 608-611.

27 U. Wehrmeister, A. L. Soldati, D. E. Jacob, T. Häger and W. Hofmeister, *J. Raman Spectrosc.*, 2010, **41**, 193-201.

28 J. R. Clarkson, T. J. Price and C. J. Adams, *J. Chem. Soc., Faraday Trans.*, 1992, **88**, 243-249.

29 D. L. Graf, *Am. Mineral.*, 1961, **46**, 1283-1316.

30 J. W. Wang and U. Becker, *Am. Mineral.*, 2009, **94**, 380-386.

31 J.Chen and L.Xiang, *Powder Technol.*, 2009, **189**, 64-69.

32 L. N. Plummer and E. Busenberg, *Geochim. Cosmochim. Acta*, 1982, **46**, 1011-1040.

33 T. Ogino, T. Suzuki and K. Sawada, *Geochim. Cosmochim. Acta*, 1987, **51**, 2757-2767.

34 Y. Xin, H. Cao, C. Liu, J. Chen, P. Liu, Y. Lu, and Z. Ling, *J. Raman Spectrosc.*, 2022, **53**, 340-355.

35 X. Zhang, P. Yu, D. Zhang, H. Zhang, X. Sun, and Y. Ma, *Mater. Lett.*, 2013, **92**, 401-404.

36 H. Wang, G. Zhao and M. Pumera, *J. Am. Chem. Soc.*, 2014, **136**, 2719-2722.

37 L. Wang, J. Chen, X. Feng, W. Zeng, R. Liu, L. Xiujing, Y. Ma and L. Wang, *RSC Advances*, 2016, **6**, 65624-65630.

38 A. A. Solovev, W. Xi, D. H. Gracias, S. M. Harazim, C. Deneke, S. Sanchez and O. G. Schmidt, *ACS Nano*, 2012, **6**, 1751-1756.

39 N. Hu, M. Sun, X. Lin, C. Gao, B. Zhang, C. Zheng, H. Xie and Q. He, *Adv. Funct. Mater.*, 2018, **28**, 1705684.

40 W. Gao, S. Sattayasamitsathit, J. Orozco and J. Wang, *J. Am. Chem. Soc.*, 2011, **133**, 11862-11864.

41 H.Wang, G. Zhao, and M. Pumera, *J. Phys. Chem. C* 2014, **118**, 5268–5274.

42 S. K. Scott, *Chemical chaos*, Clarendon Press, Oxford, 1993.

43 Y. Yoshizumi and H. Suzuki, *ACS Appl. Mater. Interfaces*, 2017, **9**, 21355-21361.